JACS
JOURNAL OF THE AMERICAN CHEMICAL SOCIETY
Article
pubs.acs.org/JACS

Thiolate Ligands as a Double-Edged Sword for CO Oxidation on CeO_2 Supported $Au_{25}(SCH_2CH_2Ph)_{18}$ Nanoclusters

Zili Wu,*[,†,‡] De-en Jiang,[†] Amanda K. P. Mann,[†] David R. Mullins,[†] Zhen-An Qiao,[†] Lawrence F. Allard,[§] Chenjie Zeng,[∥] Rongchao Jin,[∥] and Steven H. Overbury*[,†,‡]

[†]Chemical Science Division, [‡]Center for Nanophase Materials Sciences, and [§]Materials Science and Technology Division, Oak Ridge National Laboratory, Oak Ridge, Tennessee 37831, United States

[∥]Department of Chemistry, Carnegie Mellon University, 4400 Fifth Avenue, Pittsburgh, Pennsylvania 15213, United States

Supporting Information

ABSTRACT: The effect of thiolate ligands was explored on the catalysis of CeO_2 rod supported $Au_{25}(SR)_{18}$ (SR = $-SCH_2CH_2Ph$) by using CO oxidation as a probe reaction. Reaction kinetic tests, in situ IR and X-ray absorption spectroscopy, and density functional theory (DFT) were employed to understand how the thiolate ligands affect the nature of active sites, activation of CO and O_2, and reaction mechanism and kinetics. The intact $Au_{25}(SR)_{18}$ on the CeO_2 rod is found not able to adsorb CO. Only when the thiolate ligands are partially removed, starting from the interface between $Au_{25}(SR)_{18}$ and CeO_2 at temperatures of 423 K and above, can the adsorption of CO be observed by IR. DFT calculations suggest that CO adsorbs favorably on the exposed gold atoms. Accordingly, the CO oxidation light-off temperature shifts to lower temperature. Several types of Au sites are probed by IR of CO adsorption during the ligand removal process. The cationic Au sites (charged between 0 and +1) are found to play the major role for low-temperature CO oxidation. Similar activation energies and reaction rates are found for CO oxidation on differently treated $Au_{25}(SR)_{18}/CeO_2$ rod catalysts, suggesting a simple site-blocking effect of the thiolate ligands in Au nanocluster catalysis. Isotopic labeling experiments clearly indicate that CO oxidation on the $Au_{25}(SR)_{18}/CeO_2$ rod catalyst proceeds predominantly via the redox mechanism where CeO_2 activates O_2 while CO is activated on the dethiolated gold sites. These results point to a double-edged sword role played by the thiolate ligands on Au_{25} nanoclusters for CO oxidation.

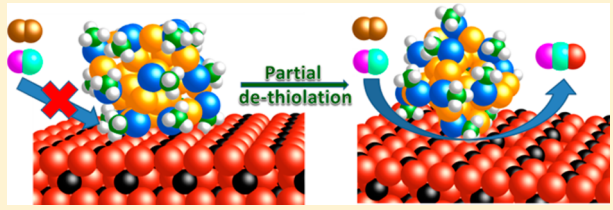

1. INTRODUCTION

Amidst the already highly active field of heterogeneous gold catalysis based on nanosized gold particles,[1,2] gold nanoclusters with a specific number of gold atoms have recently added additional spotlights into this area and opened up a new era for gold catalysis. It was shown by several research groups[3−12] that gold nanoclusters containing specific numbers of gold atoms exhibit intrinsically unique and size-specific catalytic behavior that is different from that of either atomically dispersed gold species or the traditional nanoparticle counterpart in a variety of reactions. Among gold nanoclusters, the thiolate ligand-protected gold nanoclusters (less than 2 nm in diameter), referred to as $Au_n(SR)_m$, where n and m denote the numbers of gold atoms and thiolate ligands SR ($-SCH_2CH_2Ph$), respectively, have particular potential for shedding light onto the long puzzling area of gold catalysis thanks to their atomic precision and monodispersity.[13−16] Although research on the reactivity of $Au_n(SR)_m$ nanoclusters is still in its infancy, interesting catalytic properties of $Au_n(SR)_m$ nanoclusters have been demonstrated in various types of reactions, including oxidation, hydrogenation, and coupling.[6,11] Most of the studies were conducted for liquid-phase organic reactions on free or supported gold nanoclusters, while research utilizing supported $Au_n(SR)_m$ nanoclusters for gas-phase reactions has just started to emerge.[17−20]

Interestingly, $Au_n(SR)_m$ nanoclusters are catalytically active and selective in many reactions in the liquid phase even though the surface gold atoms are coordinated with thiolate ligands, which are generally considered to be poisons in traditional metal catalysis.[21−23] Recently it was found that the removal of thiolate ligands from Au_{25} supported on carbon was beneficial for the liquid-phase reduction of 4-nitrophenol.[24] Similarly, an alkanethiol coating of a self-assembled monolayer (SAM) on a Pd film, closely related to the thiolate ligand protection of metal clusters, was found to decrease activity by 60% in the selective hydrogenation of unsaturated epoxides to saturated epoxides.[25] Considering that the alkanethiol SAM generally leaves some fraction of surface metal atoms uncoordinated while all the surface Au atoms are coordinated with thiolate ligands in the $Au_n(SR)_m$ nanoclusters, one has to wonder if there are sites available on the surface of $Au_n(SR)_m$ nanoclusters for adsorption and conversion of reactants. Quintanilla et al. found that adsorption of a thiol SAM on 10% of the sites of supported Au catalysts negatively affects the reactivity for

Received: February 21, 2014
Published: April 4, 2014

   dx.doi.org/10.1021/ja5018706 | J. Am. Chem. Soc. 2014, 136, 6111−6122

oxidation or hydrogenation reactions.[22] For thiolate ligand protected Au_{13} nanoclusters supported on TiO_2, the low-temperature CO oxidation activity was obtained only after thermal removal of the thiolate ligands.[23] Therefore, it is our primary interest to investigate the thiolate ligand effect on the catalysis of supported $Au_n(SR)_m$ nanoclusters with focus on gas-phase reactions.

To approach this goal, we select gas-phase CO oxidation as a probe reaction for two reasons. First, CO oxidation has long been utilized as a prototype reaction for understanding gold catalysis, such as the role of the Au particle size, support, and charge of the Au sites.[1,26] Second, recent studies of CO oxidation over supported $Au_n(SR)_m$ nanoclusters seem to give different views on how the ligands affect the reaction. For example, TiO_2 supported $Au_{38}(SR)_{24}$ nanoclusters did not show high activity for CO oxidation unless the thiolate ligands were removed,[20] while CeO_2 supported $Au_{25}(SR)_{18}$ and $Au_{38}(SR)_{24}$[17,18] were found to be active for low-temperature CO oxidation without the removal of any thiolate ligands. The onset of CO oxidation activity was proposed to be dependent on the O_2-pretreatment conditions rather than the thiolate ligand removal.[17,18] The nature of the oxide support (e.g., CeO_2 as opposed to TiO_2) was also assumed to cause the discrepancy,[18] but the mechanism behind the interesting CO oxidation behavior of CeO_2 supported $Au_n(SR)_m$ nanoclusters remains a mystery.

In this study, we select CeO_2 supported Au_{25} nanoclusters as an example and are motivated to reveal the role of the thiolate ligands on the CO oxidation reaction. Specifically, we use a $Au_{25}(SR)_{18}/CeO_2$ (SR = $-SCH_2CH_2Ph$; Ph = $-C_6H_5$) catalyst to address the following questions: (i) What are the active sites for CO and O_2 activation? (ii) What is the reaction mechanism for CO oxidation, i.e., Langmuir–Hinshelwood (L–H) vs Mars–van Krevelen (MvK)? (iii) How does the presence of thiolate ligands affect the reaction mechanism? Our results clearly indicate that the thiolate ligands act as a double-edged sword for the Au_{25} nanoclusters in CO oxidation: they stabilize the structural integrity of Au_{25}, yet they also block the Au sites that are needed for CO activation. CO oxidation on $Au_{25}(SR)_{18}/CeO_2$ can take place only when some of the thiolate ligands are removed from the interface between the Au nanoclusters and ceria support. With respect to the reaction mechanism, we show unambiguously that the reaction proceeds predominantly via the MvK mechanism where CeO_2 activates O_2 while CO is activated on the dethiolated gold sites and oxidized by the CeO_2 lattice oxygen.

2. EXPERIMENTAL SECTION

2.1. Materials Synthesis. $Au_{25}(SR)_{18}$ nanoclusters were synthesized using the method reported previously.[27] The synthesized $Au_{25}(SR)_{18}$ nanoclusters were characterized by both UV–vis absorption and matrix-assisted laser desorption ionization mass spectrometry (MALDI-MS). The UV–vis spectrum was collected on a Varian Cary 5000 spectrometer in the range of 300–800 nm. MALDI-MS was performed with a PerSeptive Biosystems Voyager DE super-STR time-of-flight (TOF) mass spectrometer. Cerium oxide in a rodlike morphology was chosen as the support for $Au_{25}(SR)_{18}$ nanoclusters. The synthesis of ceria rods was detailed in our recent work by using a hydrothermal method, and the rods were calcined at 673 K for 4 h prior to Au cluster impregnation.[28,29] For preparation of the $Au_{25}(SR)_{18}/CeO_2$ rod catalyst, 2 mg of $Au_{25}(SR)_{18}$ was dissolved in 5 mL of toluene, and 200 mg of CeO_2 rods was added. After the solution was stirred for 15 h at room temperature, the solid was collected by centrifugation and washed with toluene three times. Finally the sample was dried in a vacuum oven at room temperature, giving the as-synthesized catalyst. The Au loading was determined to be ~0.15 wt % via X-ray absorption measurement in transmission mode. Electron micrographs of the bare CeO_2 rods and of the $Au_{25}(SR)_{18}/CeO_2$ rod catalyst were recorded on a JEOL 2200FS FEG 200 kV scanning transmission electron microscope fitted with a CEOS GmbH (Heidelberg, Germany) aberration corrector on the probe-forming lenses. With a beam convergence semiangle of 26.5 mrad at a nominal current of 23 pA, high-angle annular dark-field (HAADF) images can be acquired at a nominal resolution in the 0.07 nm range. A standard 1 wt % Au/TiO_2 catalyst was obtained from Mintek (catalog no. 79-0165, AUROlite), designated as Mintek-Au.

2.2. CO Oxidation Test. CO oxidation over the $Au_{25}/(SR)_{18}/CeO_2$ rod sample was tested on a plug-flow, temperature-controlled microreactor system (Altamira AMI 200). The sample (ca. 32 mg), loaded into a U-shaped quartz tube (4 mm i.d.) and supported by quartz wool, was pretreated sequentially in flowing 5% O_2/He (25 mL/min) at different temperatures (423, 448, 473, 523, 573, and 673 K) for 1 h and cooled to room temperature in an O_2/He atmosphere. These treated samples were denoted as AuCe-*x*, where *x* represents the O_2-treatment temperature. For example, AuCe-423 refers to the $Au_{25}(SR)_{18}/CeO_2$ rod sample pretreated at 423 K in O_2 for 1 h. The sample was then exposed to the reaction mixture (5 mL/min 5% O_2/He + 5 mL/min 2% CO/2% Ar/He) at room temperature with a space velocity of 18 800 $cm^3/(h \cdot g_{cat})$. The system was ramped up to 413 K at a rate of 3 K/min to measure the CO light-off process. The product gas stream was analyzed with an online quadruple mass spectrometer (QMS) (OmniStar GSD-301 O2, Pfeiffer Vacuum). QMS responses were calibrated with known mixtures of CO and CO_2 at different ratios. All gases, unless specified, were provided by Air Liquide with UHP helium as the balance gas, with a moisture content of less than 1 ppm.

CO–O_2 copulse and sequential pulse experiments were manually conducted in the AMI microreactor system at 353 K using a pulse volume of 0.5 mL on the AuCe-*x* samples after different temperature O_2 pretreatments. In the copulse mode, an equal mixture of 2% CO/2% Ar/He + 5% O_2/He was pulsed repeatedly to the sample, with delays between pulses sufficient for the QMS signals of CO and CO_2 to return to baseline. In the sequential pulse mode, a 2% CO/Ar/He (10 mL/min) + He (10 mL/min) mixture was first pulsed over the sample and then a 5% O_2/He (10 mL/min) + He (10 mL/min) mixture was pulsed over the sample after the QMS signals of CO and CO_2 traces leveled off. Both pulse modes were repeated nine more times.

2.3. In Situ IR Spectroscopy. IR spectra of CO adsorption were collected using a Thermo Nicolet Nexus 670 spectrometer in diffuse reflectance mode (DRIFTS), while the exiting stream was analyzed by an OmniStar GSD-301 (Pfeiffer-Balzer) QMS. Since the removal of thiolate ligands is temperature sensitive, the $Au_{25}(SR)_{18}/CeO_2$ rod sample was first calcined in a box oven in air at different temperatures (295, 423, 473, 498, 523, 573, and 673 K) for 1 h to make the temperature consistent with that used in the reactivity test in CO oxidation on the AMI system. The box oven calcined sample was then transferred to a DRIFTS cell (HC-900, Pike Technologies, nominal cell volume of 6 cm^3) and treated in 5% O_2/He flow (25 mL/min) at the same temperatures (the actual IR cell temperature is lower than its set temperature) for another 30 min to remove adsorbed water and carbonate species formed during the sample transfer in air. The sample was then cooled to room temperature before switching to a He stream. The IR background spectrum was then collected in He flow. CO adsorption was conducted at room temperature in flow mode on the different temperature treated samples. After 2% CO/2% Ar/He was flowed for 10 min, either He or O_2/He was switched back to allow adsorbed CO to desorb or react. IR spectra were recorded continuously to follow the surface changes during the adsorption and desorption process. All reported IR spectra are difference spectra referenced to the background spectrum collected at room temperature after pretreatment but prior to CO adsorption.

2.4. In Situ Raman Spectroscopy. The $Au_{25}(SR)_{18}/CeO_2$ rod sample was pretreated in a Raman catalytic reactor (Linkam

CCR1000) in flowing 5% O_2/He (30 mL/min) at 423 and 473 K for 1 h and cooled to room temperature. Raman spectra were then collected to look for adsorbed O_2 species. Raman scattering was collected via a customized ellipsoidal mirror and directed by a fiber optics bundle (Princeton Instruments) to the spectrograph stage of a triple Raman spectrometer (Princeton Instruments Acton Trivista 555).[30] Edge filters (Semrock) were used in front of the UV−vis fiber optic bundle to block the laser irradiation. The 532 nm excitation (20 mW at the sample) was emitted from a solid-state laser (Princeton Scientific, MSL 532-50). A UV-enhanced liquid N_2-cooled charge-coupled device (CCD) detector (Princeton Instruments) was employed for signal detection. The Raman reactor sits on an XY stage (Prior Scientific, OptiScan XY system) and translates in raster mode while the spectrum is collected. The fast translation has been shown able to eliminate/minimize any laser damage of the samples. Cyclohexane was used as a standard for the calibration of the Raman shifts.

2.5. In Situ X-ray Absorption Spectroscopy (XAS). The XAS data were recorded at the Au L_{III}-edge (11 919 eV) at beamline X19a at the National Synchrotron Light Source, Brookhaven National Laboratory. A Si(111) double-crystal monochromator was used and detuned by 20% to reject higher harmonics. The X-ray absorption was measured simultaneously in transmission and fluorescence. Ion chambers for measuring I_o and I_t were filled with nitrogen and Ar, respectively. It should be noted, however, that the ceria support absorbed more than 99% of the X-ray radiation. Fluorescence was measured using a four-element silicon drift detector, model Vortex-ME4, oriented perpendicular to the upcoming beam.[31] This multielement detector not only provided enhanced sensitivity but was also energy dispersive, which enabled discrimination between the Au fluorescence and the much more intense Ce background. The Au absorption was measured out to k = 16.

The starting $Au_{25}(SR)_{18}/CeO_2$ rod sample and the Mintek-Au reference catalyst were ground to fine powders, mixed with BN, and pressed into a 13 mm diameter pellet. The typical absorbance of the analyte, $\mu(x)$, was less than 0.1. The pellets were mounted in a Nashner−Adler reaction cell.[32] Both X-ray absorption near edge structure (XANES) and extended X-ray absorption fine structure (EXAFS) spectra were collected on the sample as received and after it was heated in 20% O_2/He at 10 K min^{-1} to a sequence of increasing temperatures and held for 30 min at each temperature. Following each heating cycle, the sample was cooled to 173 K for EXAFS measurements after being purged with He. A liquid nitrogen dewar was placed on the top of the cell to enable absorption measurements at low temperature and, consequently, minimize thermal disorder effects. The programs ATHENA and ARTEMIS (available through the DEMETER software package, version 0.9.17) were used to reduce and fit the data, respectively.[33] Data reduction consisted of pre-edge subtraction, background determination, normalization, and spectral averaging.

2.6. Density Functional Theory (DFT) of CO Adsorption. Parallel, resolution-of-identity DFT calculations were performed for CO adsorption on intact and partially dethiolated $Au_{25}(SR)_{18}$ with the quantum chemistry program Turbomole, version 6.5.[34] Structural optimization was done with the PBE0 functional[35] for electron exchange and correlation and the def2-SV(P) basis sets. Effective core potentials which have 19 valence electrons and include scalar relativistic corrections were used for Au.[36] The adsorption energy, E_{ad}, is defined as $E_{ad} = E_{CO/Au} - E_{Au} - E_{CO}$, where $E_{CO/Au}$, E_{Au}, and E_{CO} are the energies of the adsorbed system, the gold cluster, and the isolated CO molecule, respectively, so a negative E_{ad} indicates a favorable interaction.

3. RESULTS AND DISCUSSION

3.1. Characterization of $Au_{25}(SR)_{18}$ Nanoclusters and the $Au_{25}(SR)_{18}/CeO_2$ Rod Catalyst. The pure nanoclusters were characterized by both UV−vis absorption (Figure 1A) and mass spectrometry (Figure 1B) analysis. The UV−vis spectrum exhibits three absorption bands at 400, 447, and 683 nm, similar to that reported for pure $Au_{25}(SR)_{18}$ nanoclusters in previous work.[27] The single m/z peak at 7391 in the mass spectrometry analysis corresponds closely to that of molecular $Au_{25}(SCH_2CH_2Ph)_{18}$ (calculated to be 7394; the deviation of 3 is due to gross calibration of the mass spectrometer), confirming that the as-prepared nanoclusters are $Au_{25}(SR)_{18}$ with atomic monodispersity. We conclude from the two analysis results that atomically precise $Au_{25}(SR)_{18}$ nanoclusters were successfully synthesized. An HAADF-STEM (STEM = scanning tunneling electron microscopy image) of the as-synthesized $Au_{25}(SR)_{18}/CeO_2$ sample is shown in Figure 1C, where an isolated Au particle is seen on the CeO_2 rod. The size of ∼1.2 nm is close to the X-ray crystallographically measured value of a $Au_{25}(SR)_{18}$ nanocluster. To better illustrate the successful synthesis and dispersion of the $Au_{25}(SR)_{18}$ nanoclusters on CeO_2 rods, a high-load (∼1 wt %) $Au_{25}(SR)_{18}/CeO_2$ sample was prepared and characterized also by HAADF-STEM imaging. Those results are shown in Figure S1 in the Supporting Information. Considering the fact that the CeO_2 rods have a large amount of defect sites[28,29] and the loading of $Au_{25}(SR)_{18}$ nanoclusters is very low, we can reasonably expect that the rod support may be helpful to anchor the gold nanoclusters. Furthermore, the cluster agglomeration could be prevented during thermal treatment because the defects in ceria were found helpful for strong bonding with metal nanoparticles.[37] This is supported by the X-ray absorption spectroscopy results shown in a later section.

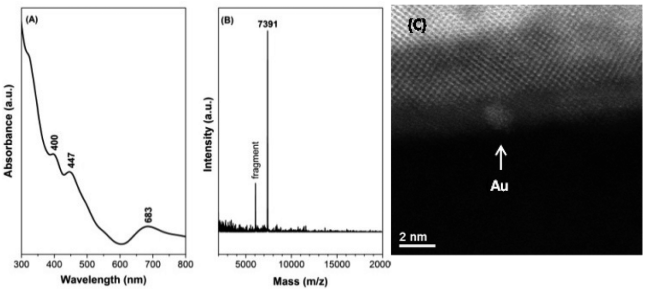

Figure 1. (A) UV−vis spectrum and (B) MS pattern of the as-synthesized $Au_{25}(SR)_{18}$ nanoclusters. (C) HAADF-STEM image of the as-synthesized $Au_{25}(SR)_{18}/CeO_2$ rod catalyst. The scale bar represents 2 nm.

3.2. CO Oxidation on the $Au_{25}(SR)_{18}/CeO_2$ Rod Catalyst. Figure 2A exhibits the light-off curves for CO oxidation over different temperature O_2-treated $Au_{25}(SR)_{18}/CeO_2$ rod catalysts. The observed CO oxidation activity in the tested temperature range is due to the presence of gold nanoclusters since the bare CeO_2 rods show activity only at temperatures above 423 K.[28] There is barely any CO oxidation activity on the as-synthesized sample. The reactivity starts to emerge only when the sample is O_2-treated at elevated temperatures. The 423 K O_2 treatment results in weak CO oxidation activity. Activity increases dramatically when the treatment temperature is increased to 448 K. The activity keeps increasing with the O_2-treatment temperature up to 523 K and then declines with further higher temperature treatment. For example, the CO conversion at 330 K is 1.7%, 24.9%, 36.3%, 39.1%, 35.3%, and 15.1% for O_2-treatment temperatures of 423, 448, 473, 523 K, 573, and 673 K, respectively. The observed trend is in general agreement with the CeO_2 nanoparticle supported $Au_{25}(SR)_{18}$ for CO oxidation reported by Nie et al.[18]

Figure 2B shows the Arrhenius plots from CO oxidation in the temperature range of 308−363 K with conversion below

dx.doi.org/10.1021/ja5018706 | J. Am. Chem. Soc. 2014, 136, 6111−6122

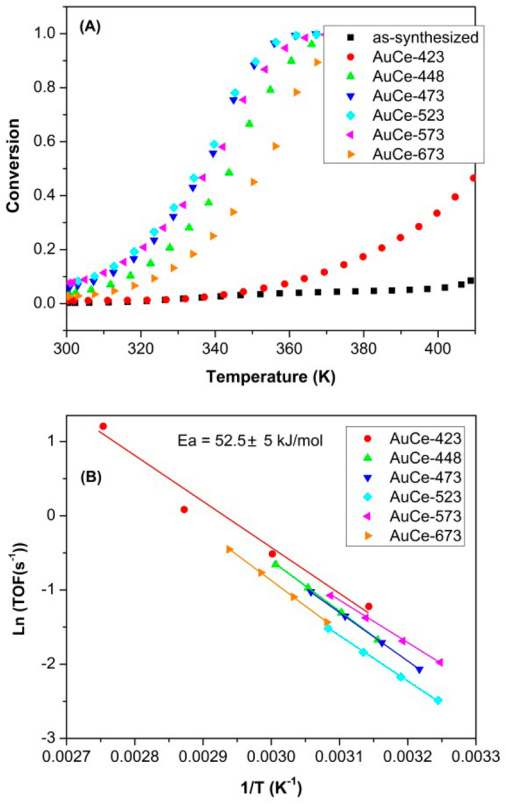

Figure 2. (A) CO oxidation light-off curves for the $Au_{25}(SR)_{18}/CeO_2$ rod catalyst pretreated in O_2 at different temperatures. The space velocity is 18 800 $cm^3/(h{\cdot}g_{cat})$. (B) Arrhenius plots from the CO oxidation data in (A) for conversions below 20%. For the AuCe-423 sample, separate CO oxidation tests were run at lower space velocity to obtain reasonable CO conversion at lower temperatures (see Figure S2, Supporting Information).

20% on the $Au_{25}(SR)_{18}/CeO_2$ rod catalyst pretreated at different temperatures in O_2. The number of Au sites used for the turnover frequency (TOF) was calculated in the following way. The maximum possible number of surface Au sites was approximated as being 50% of the total number of gold atoms, since about half of the Au atoms are at the surface of the core–shell structured $Au_{25}(SR)_{18}$ nanocluster.[6] From this maximum possible number of sites, the number of accessible sites for a given sample was then calculated on the basis of the CO adsorption observed during the IR measurements described below. The activation energy derived from these plots is 52.5 ± 5 kJ/mol for all the samples pretreated at different temperatures, indicating that CO oxidation follows a similar reaction mechanism over the differently treated catalysts. The activation energy compared well with the value of ~50 kJ/mol reported for CO oxidation on ceria supported Au catalysts.[38,39] In general, the plots show that the reaction rate (TOF) is about the same for the different temperature treated samples, e.g., around 0.5 ± 0.1 s^{-1} at a reaction temperature of 330 K. For perspective, this value can be compared with that of the best Au/CeO_2 catalyst, where the TOF at 278 K was calculated to be 0.49 s^{-1} on the basis of the number of Au atoms at the interface between Au nanoparticles and nanocrystalline CeO_2.[40]

3.3. Temperature-Dependent Removal of Thiolate Ligands. The removal of thiolate ligands from the $Au_{25}(SR)_{18}/CeO_2$ rod catalyst upon different temperature treatments was measured by both in situ IR spectroscopy (for monitoring the C–H moiety of the thiolates) and EXAFS (for monitoring the interfacial Au–S bond). C–H stretching modes are observed at 2935 and 2844 cm^{-1} in the IR spectra of the $Au_{25}(SR)_{18}/CeO_2$ rod catalyst pretreated at temperature below 523 K (Figure 3A). These bands are due to the C–H stretching in the

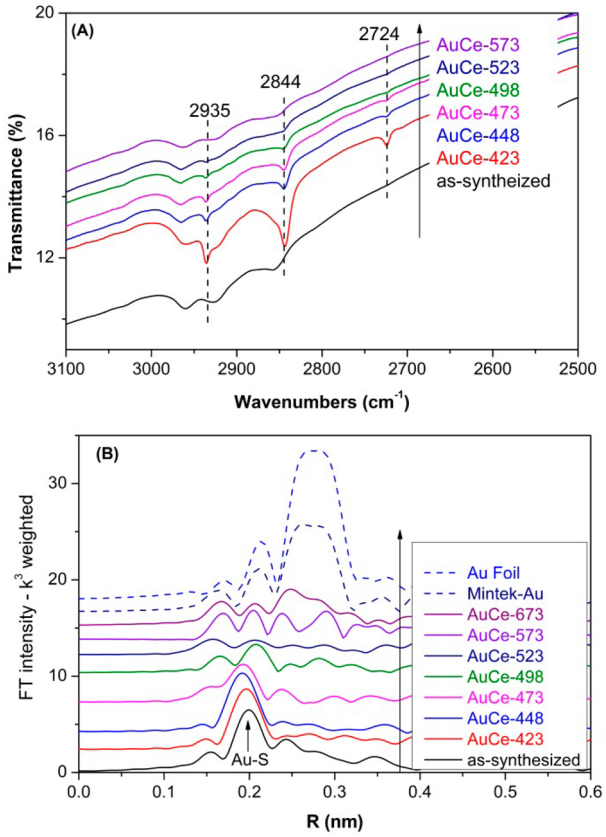

Figure 3. (A) IR background spectra of the $Au_{25}(SR)_{18}/CeO_2$ rod sample pretreated at different temperatures in O_2 and (B) EXAFS spectra of various Au samples and the $Au_{25}(SR)_{18}/CeO_2$ rod sample pretreated at different temperatures in O_2. Spectra from Au foil and the Mintek Au/TiO_2 catalyst are also shown as references.

aliphatic chain of the SCH_2CH_2Ph ligands. The absence of aromatic C–H stretching, expected between 3030 and 3100 cm^{-1}, is intriguing but was also recently noticed in the IR spectrum of unsupported $Au_{25}(SR)_{18}$ nanoclusters.[41] The IR feature at 2724 cm^{-1} is likely an overtone band of the C–H deformation mode of the aliphatic chain and thus can also be used to monitor the presence of the thiolate ligands. Interestingly, these characteristic IR features of the thiolate ligands are not prominent on the room temperature treated sample (the rather broad features in the 3000–2800 cm^{-1} region are due to instrument background), probably because they are obscured by adsorbed water on the ceria surface. These IR bands are most intense after 423 K treatment, then gradually decrease in intensity, and finally disappear at a treatment temperature of 523 K and above, implying complete removal of the thiolate ligands from the Au nanoclusters at this temperature. The temperature of 523 K is in good agreement with that for complete thiolate loss from the thermogravimetric analysis (TGA) result of bare and supported $Au_{25}(SR)_{18}$ nanoclusters.[18,42]

dx.doi.org/10.1021/ja5018706 | J. Am. Chem. Soc. 2014, 136, 6111–6122

The Au−S bond cleavage, a direct indicator of dethiolation, was followed by in situ EXAFS. The k^3-weighted EXAFS spectra are shown in Figure 3B after the $Au_{25}(SR)_{18}/CeO_2$ rod catalyst was heated in 20% O_2/He at increasing temperature. EXAFS spectra of Au foil and Mintek Au/TiO_2 are shown as references. The EXAFS spectrum from the as-synthesized $Au_{25}(SR)_{18}/CeO_2$ rod catalyst is very similar to that of unsupported $Au_{25}(SR)_{18}$ nanoclusters.[43] The prominent peak near 0.19 nm corresponds to Au−S nearest neighbors with an average Au−S distance of 0.231 nm and a coordination number of ca. 1. A similar average Au−S distance is reported for pure $Au_{25}(SR)_{18}$ nanoclusters by Simms et al.[43] Theoretically, a $Au_{25}(SR)_{18}$ has three distinct Au−Au nearest neighbor distances associated with the core, surface, and S-bonded Au.[44] Due to the low loading (0.15 wt %) of $Au_{25}(SR)_{18}$, our data did not enable us to reliably fit the EXAFS to these three shells; however, peaks associated with scattering from Au neighbors are evident between 0.2 and 0.3 nm.

After heating to 423 K, the intensity of the Au−S peak barely changes, implying no obvious loss of the thiolate ligands. However, Au−Au peaks in the 0.2−0.3 nm range show changes indicative of a structural rearrangement of the Au_{25} nanoclusters. Evidently, the structure of Au_{25} may change even after a slight loss of thiolate ligands. After heating at 448 K, the Au−S peak intensity decreases slightly, followed by a greater decrease after heating at 473 K. A slight shift of the Au−S peak to lower distance is evident for the AuCe-448 sample, implying a stronger Au−S bond compared to that of the as-synthesized sample. This observation can be well substantiated by a previous NMR study of the thermal stability of unsupported thiolated Au_{25} nanoclusters.[45] It was shown that there exist two types of Au−S binding modes with different thermal stabilities in thiolated Au_{25} nanoclusters. The Au−S bonds with lower thermal stability can be broken at a treatment temperature above 433 K, a temperature in good agreement with that in our EXAFS study. The remaining Au−S bonds are thermally more stable and thus give shorter Au−S distances as implied by the AuCe-448 EXAFS spectrum. The Au−S peak disappears upon heating at 498 K, indicating no thiolate ligands left over on the Au. This is in agreement with the loss of the C−H stretching modes as observed in the IR spectra after heating to 523 K (Figure 3A). There is little structure evident in the Au−Au region, and the Au−Au EXAFS peaks do not show an intensity increase until the treatment temperature is raised to 573 K. Interestingly, the Au−Au peaks in the 0.2−0.3 nm range are quite similar for the 673 K treated sample and the as-synthesized one. A fitting of the spectrum gives a coordination number of 8 for Au, corresponding to a Au particle size of 1−1.5 nm,[46] which is much smaller than that of the Mintek Au/TiO_2 reference sample (~2.9 ± 1.7 nm).[47] It appears that the Au nanoclusters do not increase significantly in size even after the complete removal of thiolate ligands and high-temperature treatment. A strong interaction must exist between the Au nanoclusters and CeO_2 rods to prevent their agglomeration at high temperatures such as 673 K. This point will be elaborated more in the following IR section.

3.4. Active Sites for CO Adsorption. CO adsorption on the $Au_{25}(SR)_{18}/CeO_2$ rod catalyst pretreated in O_2 at different temperatures was followed with in situ DRIFTS in an attempt to reveal the nature of Au sites. As shown in Figure 4, there is no IR band from CO adsorption on the as-synthesized sample, an indication that there are no Au sites available for CO adsorption on an intact $Au_{25}(SR)_{18}$ nanocluster. It appears that

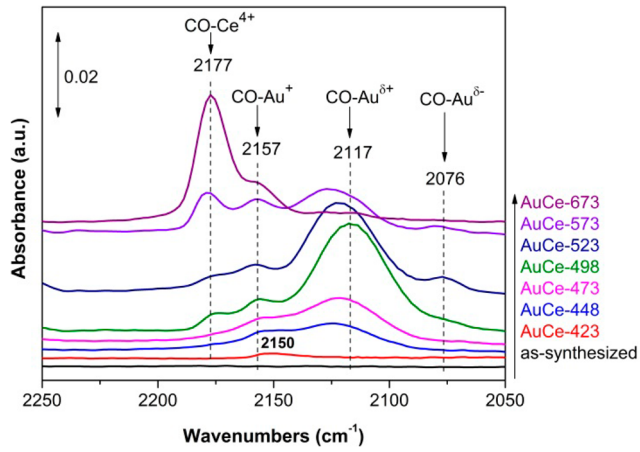

Figure 4. IR spectra of CO adsorption at room temperature on the $Au_{25}(SR)_{18}/CeO_2$ rod sample pretreated in O_2 at different temperatures.

the presence of thiolate ligands prevents CO from adsorbing on supported $Au_{25}(SR)_{18}$, although the computed structural model of $Au_{25}(SR)_{18}$ exhibits accessible Au sites.[42] This absence of CO adsorption reasonably explains the negligible CO oxidation activity on the as-synthesized sample.

O_2 treatment at 423 K leads to a very weak IR band at 2150 cm^{-1} from CO adsorption on the $Au_{25}(SR)_{18}/CeO_2$ rod catalyst, indicative of slight removal of thiolate ligands. After O_2 treatment at 448 K, a new IR band is observed at 2122 cm^{-1} in addition to the band at 2150 cm^{-1}. The band at 2122 cm^{-1} gradually shifts to 2117 cm^{-1} with increasing O_2-pretreatment temperature and maximizes in intensity after 498 K pretreatment, while a higher wavenumber band is observed at 2157 cm^{-1}. The IR bands in the range of 2150−2117 cm^{-1} can be attributed to CO adsorbed on differently charged Au ($Au^{\delta+}$, $0 < \delta < 1$) sites,[40,48−53] and the CO-band wavenumber decreases with decreasing positive charge on the Au sites. This red-shift trend is in line with the continuous dethiolation upon thermal treatment since the thiolate ligands are electron acceptors that render the surface Au atoms electron deficient.[6] The adsorbed CO molecules associated with the IR band at 2157 cm^{-1} are more resistant to conversion to CO_2 at room temperature than those associated with IR bands below 2150 cm^{-1} as discussed below, so we attribute the IR band at 2157 cm^{-1} to CO adsorbed on Au^+ which was considered active for CO oxidation only at elevated temperatures.[54] A shoulder band observed at 2177 cm^{-1} is assigned to adsorbed CO on coordinatively unsaturated Ce^{4+} sites created from the thermal dehydration of the ceria support.[28] Besides the relatively high wavenumber, this assignment is based on its increase in intensity after higher temperature pretreatment (due to further dehydration of the ceria) and its prompt loss during room temperature helium purging.[55] The weak IR band at 2076 cm^{-1} can be ascribed to CO adsorbed on negatively charged Au sites ($Au^{\delta-}$, $0 < \delta < 1$).[52,56] After pretreatment at 573 and 673 K, the IR band at 2117 cm^{-1} due to CO adsorbed on nearly neutral Au sites decreases in intensity and shifts to higher wavenumbers. Au^+ and a small proportion of $Au^{\delta+}$ ($0 < \delta < 1$) sites seem to exist after 673 K O_2 treatment. Meanwhile the band at 2177 cm^{-1} from CO adsorbed on Ce^{4+} sites evolves to dominate the spectra, due to the increased dehydration degree of CeO_2.

The presence of cationic Au sites on the $Au_{25}(SR)_{18}/CeO_2$ rod catalyst is supported by the in situ XANES spectra collected

dx.doi.org/10.1021/ja5018706 | J. Am. Chem. Soc. 2014, 136, 6111−6122

after different temperature O_2 treatments (see Figure S3 in the Supporting Information). The intensity in the "white line" region between 11 920 and 11 925 eV is higher for all the $Au_{25}(SR)_{18}/CeO_2$ rod samples than the two gold reference samples, indicating the presence of positively charged Au species, consistent with the observation from IR study of CO adsorption. The white line is more evident by subtracting the spectrum for Au foil from those of the AuCe-*x* samples (see Figure S3B), but overall, the white line intensity is much weaker than that of Au^{3+} and Au^{+} species,[4] implying that the majority of Au sites in the nanoclusters are in the metallic state. Upon heating at 573 and 673 K, the white line appears to shift slightly to lower photon energy. This shift could be due to a change in electronic structure (e.g., the increase of Au^{+} sites as indicated by IR of CO adsorption).

To reconcile the seemingly inconsistent results from IR and XANES studies of the 673 K treated $Au_{25}(SR)_{18}/CeO_2$ rod sample, i.e., the dominance of Au^{+} sites from IR spectra vs only a small amount of cationic Au sites from XANES spectra, we propose that the surface of the Au nanoclusters is covered by only a small fraction of oxidized Au (+1 charged) which can adsorb CO. It appears that the decoration of these Au^{+} sites diminishes the CO adsorption capability of the rest of the metallic Au sites. When the AuCe-673 sample is further treated with H_2 at 473 K, reappearance and dominance of the $Au^{\delta+}$ ($0 < \delta < 1$) sites on the AuCe-673 sample are evidenced by CO adsorption as exhibited in Figure S4 (Supporting Information). Thus, the reduction of the decorative Au^{+} sites can almost restore the CO adsorption capability of all the Au sites. The near recovery of the CO adsorption bands also indicates no apparent aggregation of the Au nanoclusters during 673 K treatment, consistent with the above EXAFS results.

It is interesting that various types of Au sites, as indicated by the CO IR, are present on the surface of partially and fully dethiolated $Au_{25}(SR)_{18}/CeO_2$ rod catalysts since one may expect a single type of Au site would be created upon dethiolation of the well-structured $Au_{25}(SR)_{18}$ nanoclusters. We believe the presence of these sites is related to the strong interaction between Au_{25} nanoclusters and the ceria rod, which leads to a structural change of the Au_{25} nanoclusters upon the loss of thiolate ligands. This is substantiated by the EXAFS result shown in Figure 3B which shows structural rearrangement of the Au nanoclusters upon dethiolation without obvious size growth. The strong interaction between the Au nanoclusters and the ceria rods could result in charge transfer between the two. This might be responsible for the absence of completely metallic Au sites for CO adsorption even after full dethiolation (such as the AuCe-498 and AuCe-523 samples). The Au-to-ceria charge transfer is not unusual and has been previously predicted theoretically and observed experimentally.[38,57−60]

The presence of different types of surface Au sites makes it difficult to determine the real TOF for the $Au_{25}(SR)_{18}/CeO_2$ rod catalyst in CO oxidation. However, since CO adsorption on Au is a key step for its subsequent oxidation reaction, via either the MvK or L−H channel, it is sensible that the calculated TOF based on surface Au sites accessible for CO activation shall offer a good unifying scale to compare the activity of differently dethiolated $Au_{25}(SR)_{18}/CeO_2$ rod catalysts for CO oxidation.

The integrated area of IR bands from CO adsorbed on all types of Au sites is plotted in Figure S5 (Supporting Information) as a function of the O_2-treatment temperature. The IR bands' area reaches its maximum at 498 K treatment and then decreases at higher treatment temperatures. The increase in the IR bands' area is due to the increased exposure of surface Au sites via thiolate ligand removal at temperatures below 498 K. At treatment temperatures above 498 K, the decrease is attributed to the decrease of CO-adsorbing Au sites because of the decoration by oxidized Au sites. The treatment temperature leading to the maximized IR band area coincides nicely with that for the complete removal of the thiolate ligands on the $Au_{25}(SR)_{18}$ nanoclusters as observed by in situ IR and EXAFS spectroscopy data (Figure 3A,B) and previous TGA of bare $Au_{25}(SR)_{18}$ nanoclusters.[18] Assuming that the IR absorption coefficients of CO adsorbed on the differently charged Au sites are similar, the percentage of CO-adsorbing Au sites exposed at specific treatment temperatures can be estimated on the basis of the IR bands' area normalized to that from 498 K treatment. This is also plotted in Figure S5 as a function of the pretreatment temperature. Thus, the obtained Au exposure percentage is used to calculate the turnover frequency of CO oxidation for different temperature treated $Au_{25}(SR)_{18}/CeO_2$ rod catalysts, already shown in Figure 2B. The TOF calculation is based on the assumptions that about half (13 of 25)[6] of the Au atoms are on the surface of Au_{25} nanoclusters and all the CO-accessible surface Au atoms are active once dethiolated. We point out that the thus calculated TOFs are the minimum bound since not all the surface Au atoms are active.

The total capacity of CO adsorption correlates well with the CO oxidation activity as depicted in Figure S5 (Supporting Information). The sample starts to show low-temperature CO oxidation activity and an IR band of adsorbed CO on Au sites only after 423 K O_2 pretreatment. Furthermore, the larger the CO−Au IR band intensity (i.e., the percentage of active surface Au sites exposed), the higher the activity for CO oxidation over the sample. When the CO−Au band intensity decreases, the CO oxidation activity also decreases. The nice correlation of the two observations suggests that the $Au_{25}(SR)_{18}/CeO_2$ rod catalyst is active for CO oxidation only when some of the Au atoms can adsorb/activate CO.

The interaction between CO and the $Au_{25}(SR)_{18}/CeO_2$ rod catalyst was simulated by DFT using $Au_{25}(SCH_3)_{18}^{-}$ as a model without including the CeO_2 support for simplicity. For the intact $Au_{25}(SR)_{18}^{-}$ cluster, we found that the adsorption energy of CO is about −0.08 eV. This is a rather weak physisorption. Given the entropy loss during adsorption, the adsorption free energy is in fact positive at ambient conditions for such a weak interaction. In other words, DFT predicts that CO would not adsorb on the intact $Au_{25}(SCH_3)_{18}^{-}$ cluster, in agreement with our IR spectrum for the fresh $Au_{25}(SR)_{18}/CeO_2$ rod sample which shows no sign of CO adsorption (Figure 4). To simulate the activation of the sample at an intermediate temperature such as 423−448 K, we hypothesize that a small number of thiolates are lost and some gold atoms are now exposed. Here we removed three thiolates from the same dimeric staple motif and then optimized the structure of the resulting $Au_{25}(SCH_3)_{15}$ cluster. The relaxed geometry is shown in Figure 5A. One can see that the two dethiolated gold atoms now come together (with a distance of 2.9 Å); the rest of the cluster maintains the original structure. Next we examined CO adsorption on one of the dethiolated Au atoms (Figure 5B) and found that the interaction is now much stronger with an adsorption energy of −1.12 eV and the C−Au distance is 1.95 Å, both indicating chemisorption. In the adsorbed state, the C−O bond length (at

dx.doi.org/10.1021/ja5018706 | J. Am. Chem. Soc. 2014, 136, 6111−6122

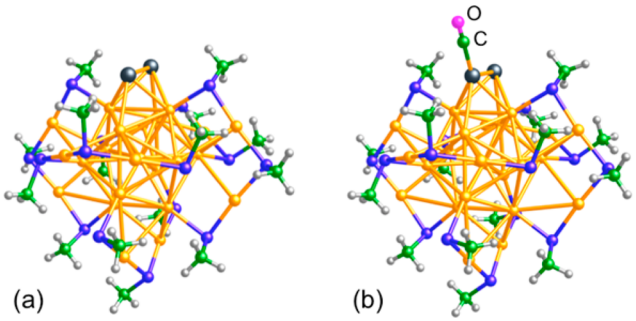

Figure 5. (A) Optimized structure of the $Au_{25}(SCH_3)_{15}$ cluster. (B) CO adsorption on the $Au_{25}(SCH_3)_{15}$ cluster. Key: Au, orange; S, blue; C, green; H, light gray; O, pink. The two dethiolated gold atoms are highlighted in dark gray.

1.134 Å) is slightly increased in comparison with the computed value for the gaseous CO (at 1.128 Å).

3.5. Active Sites for CO Oxidation. To reveal which type of Au sites (Au^+, $Au^{\delta+}$ ($0 < \delta < 1$), and $Au^{\delta-}$ ($0 < \delta < 1$)) are the active sites for CO oxidation on the O_2-pretreated $Au_{25}(SR)_{18}/CeO_2$ rod catalyst, an IR experiment was done as follows: CO was adsorbed on the 498 K O_2-treated sample at room temperature, and then desorption was conducted in flowing O_2 to follow the intensity change of the IR bands at 2078 ($CO-Au^{\delta-}$, $0 < \delta < 1$), 2117 ($CO-Au^{\delta+}$, $0 < \delta < 1$), and 2158 ($CO-Au^+$) cm^{-1}. As shown in Figure 6, the band at 2117

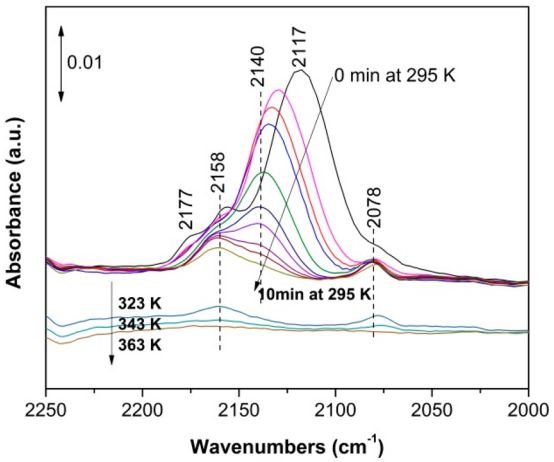

Figure 6. IR spectra obtained following adsorption of CO at 295 K onto the AuCe-498 sample. Spectra are shown as a function of time after introduction of O_2 flow at 295 K and then as temperature is increased in the O_2 flow.

cm^{-1} readily decreases in intensity and shifts to higher wavenumbers with time; meanwhile CO_2 production is observed. The IR bands in the range of 2117–2140 cm^{-1} disappear after 10 min of O_2/He flow at room temperature. However, the bands at 2078 and 2158 cm^{-1} stay relatively unchanged with time on stream at room temperature and only disappear upon heating. The contrast clearly suggests that the partially positively charged Au species ($Au^{\delta+}$ ($0 < \delta < 1$)) are the major active sites for CO oxidation on the $Au_{25}(SR)_{18}/CeO_2$ rod catalyst at low temperatures while the Au sites in +1 and $-\delta$ ($0 < \delta < 1$) charged states can contribute to CO oxidation only above room temperature. This is in general agreement with other supported Au nanocatalysts where the more positively charged the Au species are, the less active they are for low-temperature CO oxidation.[48,49,53,54,56] The trend here is different from that of the previous study of Au nanoparticles supported on nanocrystalline CeO_2[61] where cationic Au species were found more active than metallic Au for CO oxidation.

It is also essential to follow the nature of the Au sites during CO oxidation catalysis. $Au_{25}(SR)_{18}/CeO_2$ rod samples pretreated at two different temperatures by O_2 were investigated for CO adsorption before, during, and after CO oxidation. Figure S6 (Supporting Information) compares such IR spectra for 423 and 498 K O_2-treated samples. In both cases, the frequency of adsorbed CO does not change before and after CO oxidation, indicating that the nature of Au sites is not altered after CO oxidation. During CO oxidation at 373 K, no obvious CO–Au band can be observed for the 423 K treated sample while an IR band due to adsorbed CO is observed at a frequency slightly higher than 2117 cm^{-1} on the 498 K treated sample. These observations suggest that the partially charged Au sites are indeed the active sites for CO oxidation on both partially and fully dethiolated Au_{25}/CeO_2 rod samples.

3.6. Active Sites for O_2 Adsorption. Raman spectroscopy (laser excitation at 532 nm) was employed to detect if there is any adsorbed O_2 species generated from the O_2 pretreatment of the $Au_{25}(SR)_{18}/CeO_2$ rod sample. As shown in Figure S7 (Supporting Information), there are no observable Raman bands in the spectral region of 800–1600 cm^{-1} expected from adsorbed O_2 species[29,61] at room temperature on the samples that are O_2-pretreated at 423 or 473 K, indicating that either no special adsorbed O_2 species is produced from the O_2 pretreatment or its amount is below the detection limit of Raman spectroscopy. O_2 flow or CO oxidation at room temperature over the two differently treated samples gives Raman spectra similar to those in Figure S7; i.e., no adsorbed oxygen species is observable. Thus, we find no evidence for the presence of adsorbed O_2 species for CO oxidation over dethiolated $Au_{25}(SR)_{18}/CeO_2$ rod samples.

3.7. CO Oxidation Mechanism. Several isotopic labeling experiments were carried out to reveal the CO oxidation mechanism. We choose to illustrate this with a $Au_{25}(SR)_{18}/CeO_2$ rod sample that was pretreated in O_2 at 423 K because thus treated sample still has most of the thiolate ligands attached.

3.7.1. CO Oxidation with $^{18}O_2$. The sample was pretreated at 423 K and cooled to room temperature in $^{16}O_2$. Then a CO + $^{18}O_2$ light-off process was carried out after $^{16}O_2$ was purged out with He. The CO_2 isomers, $C^{16}O^{16}O$, $C^{16}O^{18}O$, and $C^{18}O^{18}O$, were monitored by the online QMS, and the profiles are shown in Figure 7A as a function of temperature. The CO_2 production is dominated by $C^{16}O^{16}O$ in the temperature range of 295–420 K. A small contribution from $C^{16}O^{18}O$ is observed only as the temperature rises above 360 K, while $C^{18}O^{18}O$ production is barely observable. The growing contribution from $C^{16}O^{18}O$ at higher temperature is due to the reaction of CO with lattice ^{18}O replenished by the gas-phase $^{18}O_2$. The observation of only $C^{16}O^{16}O$ at the initial stage of the CO oxidation light-off process and its dominance over the tested temperature range indicate that CO reacts with either $Ce^{16}O_2$ lattice oxygen or adsorbed $^{16}O_2$ generated from O_2 pretreatment at 423 K. We can rule out the latter, because of the above Raman result (Figure S7, Supporting Information). The following experiment also confirms that no adsorbed O_2

dx.doi.org/10.1021/ja5018706 | J. Am. Chem. Soc. 2014, 136, 6111–6122

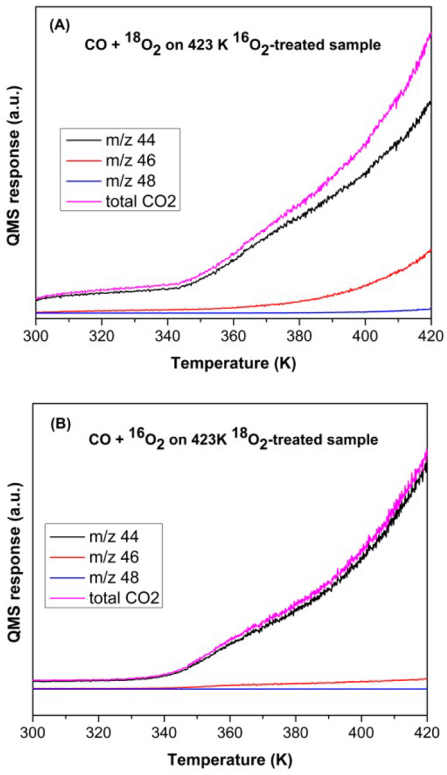

Figure 7. Isotopic exchange experiments during CO oxidation on the AuCe-423 sample: (A) CO + $^{18}O_2$ on the 423 K $^{16}O_2$-treated sample; (B) CO + $^{16}O_2$ on the 423 K $^{18}O_2$-treated sample.

species resulted from the O_2 pretreatment of the $Au_{25}(SR)_{18}/CeO_2$ rod sample at 423 K.

3.7.2. CO Oxidation on the $^{18}O_2$-Pretreated Sample. The as-synthesized $Au_{25}(SR)_{18}/CeO_2$ rod sample was pretreated at 423 K and cooled to room temperature in $^{18}O_2$. Then the CO + $^{16}O_2$ light-off process was carried out after $^{18}O_2$ was purged out with He at room temperature. As shown in Figure 7B, CO_2 production is solely the $C^{16}O^{16}O$ isomer. The result clearly indicates that the $^{18}O_2$ pretreatment at 423 K does not lead to any adsorbed oxygen species that would oxidize CO to CO_2 at low temperature on the $Au_{25}(SR)_{18}/CeO_2$ rod catalyst.

3.7.3. Isotopic Switch during Steady-State CO Oxidation. After the $Au_{25}(SR)_{18}/CeO_2$ rod sample was pretreated at 423 K with $^{16}O_2$, CO oxidation was first carried out at 353 K with $^{18}O_2$. As shown in Figure S8 (Supporting Information), a slight delay of $C^{16}O^{18}O$ production is observed relative to the $C^{16}O^{16}O$ production, with the former stabilizing with time on stream while the latter undergoes a maximum and then decreases. $C^{18}O^{18}O$ is also seen at a further delayed time with much less content than the other two isomers, whose production is probably from the isotopic exchange between lattice ^{18}O and the other two CO_2 isomers. After purging with He and switching to CO oxidation with $^{16}O_2$, the production of all three CO_2 isomers is observed simultaneously, with $C^{16}O^{18}O$ and $C^{18}O^{18}O$ quickly diminishing with time on stream.

The observations from the isotopic exchange experiments clearly imply that CO reacts with lattice oxygen of CeO_2, instead of directly with the cofed O_2, to form CO_2 starting from room temperature; namely, CO oxidation proceeds via an MvK mechanism. The cofed O_2 enters into the reaction only after a delay, due to activation of the O_2 at lattice vacancies (Figure S8, Supporting Information). To our knowledge, this is the first unambiguous experimental evidence for the operation of the MvK mechanism in *low-temperature CO oxidation* on Au/CeO_2 catalysts. This is well supported by recent DFT studies of CO oxidation on a ceria supported Au system[60,62−65] where the ceria lattice oxygen is favorably involved in direct CO oxidation. The MvK mechanism was demonstrated for CO oxidation on CeO_2 rod supported Au nanoparticles, but at much higher temperature (573 K).[66] For low-temperature (<423 K) CO oxidation, only one study proposed the MvK mechanism for Au/CeO_2 where temporal analysis of products (TAP) was used to reveal the nature of active oxygen species,[67,68] but other experimental studies suggested otherwise. Through an in situ Raman spectroscopy study of CO oxidation on nanocrystalline CeO_2 supported Au nanoparticles, Guzman et al.[61] concluded that the gas-phase O_2 was activated by the ceria support, i.e., adsorbed O_2 species, for CO oxidation while the lattice O did not participate in direct CO oxidation. Lee et al.[69] studied Au nanoparticles supported on ceria nanoshapes for CO oxidation by monitoring the oxygen vacancy concentration change during the reaction with Raman spectroscopy. They indicated that the ceria lattice oxygen does not contribute to CO oxidation below 323 K.

Participation of lattice oxygen may be related to the uniqueness of Au_{25} nanoclusters and their interaction with the CeO_2 rods, which leads to the activation of lattice oxygen of CeO_2 rods. CO oxidation on bare CeO_2 rods also follows the MvK mechanism,[28] although at a much higher light-off temperature (>423 K) than for the O_2-treated $Au_{25}(SR)_{18}/CeO_2$ rod samples. The presence of Au_{25} nanoclusters apparently promotes the reactivity of the lattice oxygen of CeO_2 rods. This is supported by the results from CO-TPR (Figure S9, Supporting Information) of the different temperature O_2-treated $Au_{25}(SR)_{18}/CeO_2$ rod samples. Although CO_2 evolves only above 400 K from bare CeO_2 rods in CO-TPR,[28] CO_2 production starts at 320 K or lower on the $Au_{25}(SR)_{18}/CeO_2$ rod samples pretreated at 423 K and above. The slight production of CO_2 above 340 K on the as-synthesized sample is due to decomposition of native carbonate species adsorbed on the CeO_2 rods. In general, the more the thiolate ligands are removed, the higher the reactivity of the lattice oxygen of ceria rods. The production temperature of CO_2 in the CO-TPR is in general alignment with the trend of the CO oxidation light-off process (Figure 2), a good indication that the lattice oxygen participates in CO oxidation on a $Au_{25}(SR)_{18}/CeO_2$ rod sample. The increased reactivity of ceria lattice oxygen, presumably at the interface of Au_{25} and CeO_2, is attributed to two benefits brought about by $Au_{25}(SR)_{18}$ nanoclusters: facile activation of CO and generation of Ce^{3+} (oxygen vacancies) via charge transfer from Au to ceria.[38,57,60] Both factors would result in enhanced reducibility of ceria[28] and thus the much lower light-off temperature for CO oxidation on the $Au_{25}(SR)_{18}/CeO_2$ rod catalyst. This type of Au-assisted MvK mechanism was also suggested for CO oxidation on other supported Au catalysts such as Au/TiO_2,[68,70] Au/FeO_x,[71] $Au/FePO_4$,[53] etc.

3.8. Effect of Thiolate Ligands on the CO Oxidation Mechanism. The effect of the thiolate ligands on the CO oxidation pathways and reaction kinetics over the $Au_{25}(SR)_{18}/CeO_2$ rod catalyst is illustrated below.

3.8.1. Effect of Thiolate Ligands on CO oxidation Pathways. To quantify how much the redox route contributes to the CO oxidation over the $Au_{25}(SR)_{18}/CeO_2$ rod catalyst, a

dx.doi.org/10.1021/ja5018706 | J. Am. Chem. Soc. 2014, 136, 6111−6122

$CO-O_2$ copulse and sequential CO and CO_2 pulses were conducted at 353 K over the sample pretreated by O_2 at different temperatures. Due to the transient adsorption of O_2, CO can react only with the lattice oxygen in the sequential pulse, while in the copulse mode CO can react with both lattice oxygen and any possible adsorbed O_2. Comparison of the two sets of experiments should give an estimation of the contribution of the redox route to the total CO oxidation. In the experiments summarized in Figure 8, CO oxidation was conducted on the samples at 353 K for an extended period until the CO_2 production was stabilized before the pulse experiments were conducted. In this way, the catalyst surface is saturated with carbonate species formed from CO/CO_2 interaction with ceria so that any CO_2 produced from the pulses should leave the catalyst surface and be monitored by the online mass spectrometer. Figure 8A compares the CO_2 production of 10 pulses from the copulse and sequential pulses of CO and O_2 over the AuCe-473 sample. The CO_2 amount from sequential pulses is about 80% of that from the copulse, confirming the dominant role of the redox mechanism in CO oxidation. Quantification was also done on $Au_{25}(SR)_{18}/CeO_2$ rod samples pretreated at different temperatures with O_2, and the result is shown in Figure 8B. For all stages of dethiolation, the MvK mechanism is responsible for about 80% of the CO oxidation on the $Au_{25}(SR)_{18}/CeO_2$ rod catalyst. Recent DFT studies[60,63−65] of CO oxidation on ceria supported Au clusters suggested that the MvK mechanism contributes significantly to CO oxidation activity when the ceria is stepped or nanosized with vacancies[64] or terminated by (110) facets.[63] This is consistent with these experimental results since CeO_2 rods are highly defective and could be partially terminated by (110) facets.[29]

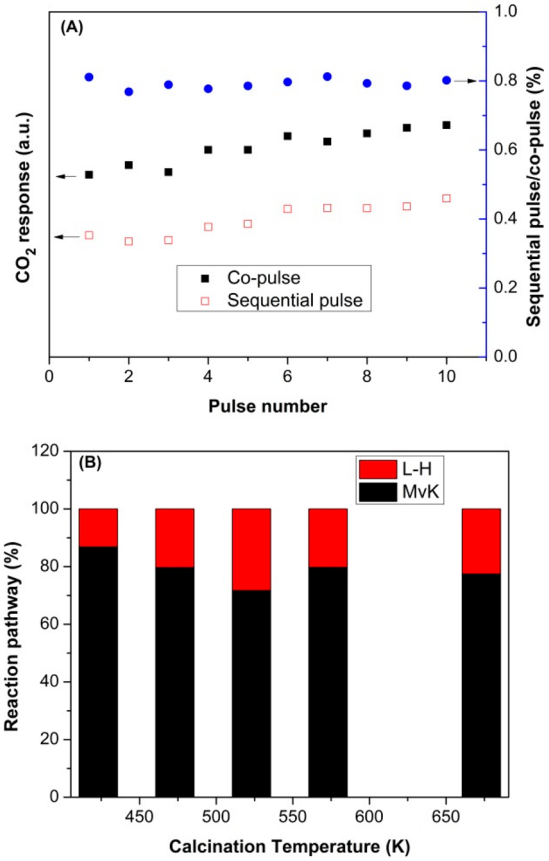

Figure 8. (A) Amount of CO_2 production during the copulse (black squares) and sequential pulses (red squares) of CO and O_2 at 353 K on the $Au_{25}(SR)_{18}/CeO_2$ rod sample pretreated at 473 K in O_2 along with their ratios (blue squares). (B) Percentage of MvK and L−H reaction pathways on $Au_{25}(SR)_{18}/CeO_2$ rod catalysts pretreated at different temperatures with O_2.

It is notable that the contribution from the L−H mechanism is the largest on the 523 K O_2-pretreated sample, ca. 28%. Since thiolate ligands are completely removed after this temperature pretreatment and the Au nanoclusters do not change apparently in size according to EXAFS results (Figure 3B), it appears that the exposed surface Au sites may be able to activate O_2 and thus contribute to the L−H mechanism for CO oxidation. This is in line with a recent DFT study of O_2 activation on $Au_{25}(SR)_{18}$ where O_2 is found to favorably bind with Au atoms only when the thiolate ligands are partially removed.[72] On the basis of a DFT+U study of CO oxidation on Au_{13} supported on CeO_2,[65] Kim et al. also showed that an L−H pathway for CO oxidation can take place by coadsorbed CO and O_2 on the undercoordinated Au atoms. These authors also suggested a new pathway where CO is oxidized by O_2 adsorbed on the $Au-Ce^{3+}$ bridge site.[65] No evidence is found for the existence of this mechanism in our catalytic system, but its contribution, if present, would be much smaller compared to that of the MvK channel.

In the MvK mechanism, CO adsorbed on the Au sites of the $Au_{25}(SR)_{18}/CeO_2$ rod catalyst reacts with the lattice oxygen of CeO_2 to form CO_2, while the gas-phase O_2 replenishes the consumed lattice oxygen. Considering that only less than 5% of the surface Au sites are available for CO adsorption on the sample after 423 K O_2 pretreatment (Figure S5, Supporting Information), these Au sites have to be around the perimeter area so that the adsorbed CO can have a good chance to react with the lattice oxygen of CeO_2. Likewise, the active lattice oxygen should be located at the perimeter area. Therefore, the thiolate ligand removal most likely starts at the interface between the $Au_{25}(SR)_{18}$ nanoclusters and the CeO_2 support and then progresses to the top surface of the Au nanoclusters. This is reasonable because the highly reactive lattice oxygen of ceria rods[28] may assist the removal of the thiolate ligands of the $Au_{25}(SR)_{18}$ nanoclusters at temperatures below the thermal desorption point of the thiolate ligands from the gold nanoclusters. As schematically shown in Scheme 1, it appears

Scheme 1. CO Oxidation Mechanism on Intact, Partially and Fully Dethiolated $Au_{25}(SR)_{18}/CeO_2$ Rod Catalysts

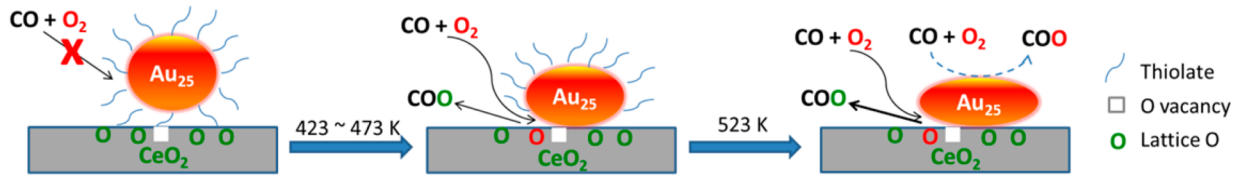

dx.doi.org/10.1021/ja5018706 | J. Am. Chem. Soc. 2014, 136, 6111−6122

that the removal of thiolate ligands controls the contribution of the two reaction mechanisms. Initial removal permits the operation of almost solely the MvK route at the triple-phase boundary, thiolates, Au, and CeO_2. Further removal of thiolates opens up more surface Au sites which could participate in CO oxidation via the L−H route[65] in addition to the MvK route at the interface. At higher treatment temperatures, the Au nanoclusters may wet the ceria rods, and thus, the contribution of MvK increases again.

Surface hydroxyls are known to contribute to CO oxidation on supported Au nanoparticles as described in a most recent review.[73] Considering that the reaction mixtures, $CO-O_2-He$, contain a very low level of moisture (<1 ppm) in our work, we believe that the contribution of hydroxyls for CO oxidation is limited on the $Au_{25}(SR)_{18}/CeO_2$ rod catalyst.

3.8.2. Effect of Thiolate Ligands on CO Oxidation Kinetics. Figure 2B shows that the activation energy and reaction rate (TOF) of CO oxidation are not sensitive to the coverage of thiolate ligands on the $Au_{25}(SR)_{18}/CeO_2$ rod catalyst. As described above, the TOF is calculated on the basis of the assumption that the IR absorption coefficients from adsorbed CO are similar on all Au sites. Actually, it has been shown that the absorption coefficient of CO adsorbed on more positively charged Au species is smaller than that of CO on less positively charged and metallic Au because the π back-donation in $CO-Au^0$ enhances the IR band intensity more than the σ bond does in $CO-Au^{\delta+}$ ($\delta > 0$).[51,74] Although there is no quantitative value for the absorption coefficient of CO on differently charged Au sites on CeO_2, it does not appear the difference is significant due to the fact that σ contribution is always present in CO interaction with Au.[51] This was shown in the case of Au/SiO_2 where the IR band area increase from CO adsorption on cationic Au to metallic Au (increase in π bond) is less than 50%.[48] Therefore, we expect that even an accurate correction for the IR coefficients would not significantly affect the calculation of the numbers of Au sties and therefore the TOFs for the Au_{25}/CeO_2 rod catalyst with/without the presence of thiolate ligands. It is thus concluded that the thiolate ligands do not seem to pose an apparent positive or negative effect on the reaction kinetics of the *accessible* Au sites for CO oxidation. The independence of both the activation energy and reaction rate on the thiolate ligand coverage suggests that the thiolate ligands have a merely geometric blocking rather than electronic effect on Au catalysis. The long-range electronic or the ensemble effect, observed in sulfur poisoning of other metal catalysts,[75] does not seem to work in the case of thiolate-protected Au nanoclusters for CO oxidation.

3.8.3. Comment on the Thiolate Ligand Effect for Liquid- and Gas-Phase Reactions. It is worthwhile to comment that the intact $Au_{25}(SR)_{18}$ nanoclusters, either supported or unsupported, are quite active for a variety of reactions in the aqueous phase even though the surface Au atoms are completely coordinated with thiolate ligands.[6] This is quite different from what we found in this study for gas-phase reaction where the thiolate ligands have to be at least partially removed to allow Au_{25} nanoclusters to be active for CO oxidation. The difference is probably due to the fact that the thiolate ligands can be flexible or even in an on-and-off dynamic state in the presence of solvent so that some of the Au sites can be accessible to reactants.[6,42] In the gas phase, the large thiolate ligands lose their flexibility and may be rigidly bound to the shell of the Au_{25} nanoclusters, thus preventing reactant from adsorbing and further reaction. It would be interesting to compare the same reaction but in both liquid- and gas-phase conditions to understand how the thiolate ligands affect the catalysis by $Au_n(SR)_m$ nanoclusters. Au nanoclusters with uncoordinated Au atoms, such as the recently reported diphosphine-stabilized Au_{22}[76] nanoclusters, are supposed to be active for catalysis without the need to remove the ligands. Research on such gold nanoclusters for gas-phase reactions is under way in our laboratory.

4. CONCLUSION

The effect of thiolate ligands on the catalysis of CeO_2 rod supported $Au_{25}(SR)_{18}$ has been probed by CO oxidation via a reaction test, in situ IR and X-ray absorption (EXAFS and XANES) spectroscopy, isotopic labeling, and DFT calculation. It was concluded that the thiolate ligands act as a double-edged sword for the Au_{25} nanoclusters for CO oxidation in the gas phase. Specifically, the thiolate ligands maintain the structural integrity of $Au_{25}(SR)_{18}$, but disable all Au sites from adsorbing CO, and thus, the intact catalyst is not active for CO oxidation. Partial removal of thiolate ligands, starting from the interface between $Au_{25}(SR)_{18}$ and CeO_2 at treatment temperatures of 423 K and above, is required for CO activation and thus the onset of low-temperature CO oxidation on the $Au_{25}(SR)_{18}/CeO_2$ rod catalyst. The removal of thiolate ligands on the $Au_{25}(SR)_{18}/CeO_2$ rod catalyst results in three types of Au sites: $Au^{\delta+}$ ($0 < \delta < 1$), Au^+, and $Au^{\delta-}$ ($0 < \delta < 1$). The former is active for CO oxidation at low temperature, while the latter two are active at elevated temperatures. The thiolate ligands seem to behave simply as site-blocking agents, without impacting the reactivity of the *accessible* Au sites. CO oxidation takes place predominantly at the interface among the thiolate ligands, Au, and CeO_2 on the partially dethiolated $Au_{25}(SR)_{18}/CeO_2$ rod catalyst via the MvK mechanism. CO is activated by accessible Au sites, while CeO_2 activates O_2, and the lattice O participates in CO oxidation. The removal of thiolate ligands opens up an additional minor channel for CO oxidation on the Au nanoclusters supported on CeO_2 rods via the L−H mechanism, where both CO and O_2 are activated by the exposed Au sites. The results here provide fundamental implications for how the ligand-protected Au nanoclusters can be further investigated as efficient catalysts for gas-phase reactions.

■ ASSOCIATED CONTENT

Supporting Information

Additional STEM images, CO oxidation activity data, IR spectra, XANES spectra, CO-TPR profiles, and isotopic exchange results (Figure S1−S9). This material is available free of charge via the Internet at http://pubs.acs.org.

■ AUTHOR INFORMATION

Corresponding Authors

wuz1@ornl.gov
overburysh@ornl.gov

Notes

The authors declare no competing financial interest.

■ ACKNOWLEDGMENTS

This work was supported by the U.S. Department of Energy, Office of Science, Office of Basic Energy Sciences, Chemical Sciences, Geosciences, and Biosciences Division. Part of the work including the Raman study was conducted at the Center

for Nanophase Materials Sciences, which is sponsored at Oak Ridge National Laboratory (ORNL) by the Scientific User Facility Division, Office of Basic Energy Sciences, U.S. Department of Energy. Use of the National Synchrotron Light Source, Brookhaven National Laboratory, was supported by the U.S. Department of Energy, Office of Science, Office of Basic Energy Sciences, under Contract DE-AC02-98CH10886 with additional support through the Synchrotron Catalysis Consortium under Grant DE-FG02-05ER15688. The research was supported in part by the appointment for A.K.P.M. and Z.-A.Q. to the ORNL Postdoctoral Research Associates Program, administered jointly by ORNL and the Oak Ridge Associated Universities. R.J. acknowledges research support from the U.S. Department of Energy, Office of Basic Energy Sciences, Grant DE-FG02-12ER16354.

REFERENCES

(1) Haruta, M.; Kobayashi, T.; Sano, H.; Yamada, N. *Chem. Lett.* **1987**, 405.
(2) Hashmi, A. S. K. *Science* **2012**, *338*, 1434.
(3) Gates, B. C. *Chem. Commun.* **2013**, *49*, 7876.
(4) Aguilar-Guerrero, V.; Lobo-Lapidus, R. J.; Gates, B. C. *J. Phys. Chem. C* **2009**, *113*, 3259.
(5) Flytzani-Stephanopoulos, M.; Gates, B. C. *Annu. Rev. Chem. Biomol.* **2012**, *3*, 545.
(6) Li, G.; Jin, R. C. *Acc. Chem. Res.* **2013**, *46*, 1749.
(7) Corma, A. *Nat. Chem.* **2013**, *5*, 775.
(8) Xie, S. H.; Tsunoyama, H.; Kurashige, W.; Negishi, Y.; Tsukuda, T. *ACS. Catal.* **2012**, *2*, 1519.
(9) Tsukuda, T. *Bull. Chem. Soc. Jpn.* **2012**, *85*, 151.
(10) Oliver-Meseguer, J.; Cabrero-Antonino, J. R.; Dominguez, I.; Leyva-Perez, A.; Corma, A. *Science* **2012**, *338*, 1452.
(11) Zhu, Y.; Qian, H. F.; Das, A.; Jin, R. C. *Chin. J. Catal.* **2011**, *32*, 1149.
(12) Herzing, A. A.; Kiely, C. J.; Carley, A. F.; Landon, P.; Hutchings, G. J. *Science* **2008**, *321*, 1331.
(13) Zhu, Y.; Qian, H. F.; Jin, R. C. *Chem.—Eur. J.* **2010**, *16*, 11455.
(14) Jin, R. C.; Qian, H. F.; Wu, Z. K.; Zhu, Y.; Zhu, M. Z.; Mohanty, A.; Garg, N. *J. Phys. Chem. Lett.* **2010**, *1*, 2903.
(15) Maity, P.; Xie, S. H.; Yamauchi, M.; Tsukuda, T. *Nanoscale* **2012**, *4*, 4027.
(16) Chaki, N. K.; Negishi, Y.; Tsunoyama, H.; Shichibu, Y.; Tsukuda, T. *J. Am. Chem. Soc.* **2008**, *130*, 8608.
(17) Nie, X. T.; Zeng, C. J.; Ma, X. G.; Qian, H. F.; Ge, Q. J.; Xu, H. Y.; Jin, R. C. *Nanoscale* **2013**, *5*, 5912.
(18) Nie, X. T.; Qian, H. F.; Ge, Q. J.; Xu, H. Y.; Jin, R. C. *ACS Nano* **2012**, *6*, 6014.
(19) Ma, G. C.; Binder, A.; Chi, M. F.; Liu, C.; Jin, R. C.; Jiang, D. E.; Fan, J.; Dai, S. *Chem. Commun.* **2012**, *48*, 11413.
(20) Gaur, S.; Miller, J. T.; Stellwagen, D.; Sanampudi, A.; Kumar, C. S. S. R.; Spivey, J. J. *Phys. Chem. Chem. Phys.* **2012**, *14*, 1627.
(21) Somorjai, G. A. *J. Catal.* **1972**, *27*, 453.
(22) Haider, P.; Urakawa, A.; Schmidt, E.; Baiker, A. *J. Mol. Catal. A* **2009**, *305*, 161.
(23) Menard, L. D.; Xu, F. T.; Nuzzo, R. G.; Yang, J. C. *J. Catal.* **2006**, *243*, 64.
(24) Shivhare, A.; Chevrier, D. M.; Purves, R. W.; Scott, R. W. J. *J. Phys. Chem. C* **2013**, *117*, 20007.
(25) Marshall, S. T.; O'Brien, M.; Oetter, B.; Corpuz, A.; Richards, R. M.; Schwartz, D. K.; Medlin, J. W. *Nat. Mater.* **2010**, *9*, 853.
(26) Green, I. X.; Tang, W. J.; Neurock, M.; Yates, J. T. *Science* **2011**, *333*, 736.
(27) Zhu, M.; Lanni, E.; Garg, N.; Bier, M. E.; Jin, R. *J. Am. Chem. Soc.* **2008**, *130*, 1138.
(28) Wu, Z. L.; Li, M. J.; Overbury, S. H. *J. Catal.* **2012**, *285*, 61.
(29) Wu, Z. L.; Li, M. J.; Howe, J.; Meyer, H. M.; Overbury, S. H. *Langmuir* **2010**, *26*, 16595.
(30) Wu, Z. L.; Dai, S.; Overbury, S. H. *J. Phys. Chem. C* **2010**, *114*, 412.
(31) Woicik, J. C.; Ravel, B.; Fischer, D. A.; Newburgh, W. J. *J. Synchrotron Radiat.* **2010**, *17*, 409.
(32) Nashner, M. S.; Frenkel, A. I.; Adler, D. L.; Shapley, J. R.; Nuzzo, R. G. *J. Am. Chem. Soc.* **1997**, *119*, 7760.
(33) Ravel, B.; Newville, M. *J. Synchrotron Radiat.* **2005**, *12*, 537.
(34) Ahlrichs, R.; Bar, M.; Haser, M.; Horn, H.; Kolmel, C. *Chem. Phys. Lett.* **1989**, *162*, 165.
(35) Adamo, C.; Barone, V. *J. Chem. Phys.* **1999**, *110*, 6158.
(36) Andrae, D.; Haussermann, U.; Dolg, M.; Stoll, H.; Preuss, H. *Theor. Chim. Acta* **1990**, *77*, 123.
(37) Farmer, J. A.; Campbell, C. T. *Science* **2010**, *329*, 933.
(38) Zhou, Z.; Flytzani-Stephanopoulos, M.; Saltsburg, H. *J. Catal.* **2011**, *280*, 255.
(39) Aguilar-Guerrero, V.; Gates, B. C. *J. Catal.* **2008**, *260*, 351.
(40) Carrettin, S.; Concepcion, P.; Corma, A.; Nieto, J. M. L.; Puntes, V. F. *Angew. Chem., Int. Ed.* **2004**, *43*, 2538.
(41) Farrag, M.; Tschurl, M.; Dass, A.; Heiz, U. *Phys. Chem. Chem. Phys.* **2013**, *15*, 12539.
(42) Li, G.; Jiang, D. E.; Liu, C.; Yu, C. L.; Jin, R. C. *J. Catal.* **2013**, *306*, 177.
(43) Simms, G. A.; Padmos, J. D.; Zhang, P. *J. Chem. Phys.* **2009**, 131.
(44) MacDonald, M. A.; Chevrier, D. M.; Zhang, P.; Qian, H. F.; Jin, R. C. *J. Phys. Chem. C* **2011**, *115*, 15282.
(45) Wu, Z. K.; Jin, R. C. *ACS Nano* **2009**, *3*, 2036.
(46) Frenkel, A. I.; Hills, C. W.; Nuzzo, R. G. *J. Phys. Chem. B* **2001**, *105*, 12689.
(47) Saavedra, J.; Powell, C.; Panthi, B.; Pursell, C. J.; Chandler, B. D. *J. Catal.* **2013**, *307*, 37.
(48) Wu, Z. L.; Zhou, S. H.; Zhu, H. G.; Dai, S.; Overbury, S. H. *J. Phys. Chem. C* **2009**, *113*, 3726.
(49) Wu, Z. L.; Zhou, S. H.; Zhu, H. G.; Dai, S.; Overbury, S. H. *Chem. Commun.* **2008**, 3308.
(50) Guan, Y. J.; Ligthart, D. A. J. M.; Pirgon-Galin, O.; Pieterse, J. A. Z.; van Santen, R. A.; Hensen, E. J. M. *Top. Catal.* **2011**, *54*, 424.
(51) Hadjiivanov, K.; Vayssilov, G. *Advances in Catalysis*; Academic Press: San Diego, CA, 2002; Vol. *47*, p 308.
(52) Manzoli, M.; Boccuzzi, F.; Chiorino, A.; Vindigni, F.; Deng, W. L.; Flytzani-Stephanopoulos, M. *J. Catal.* **2007**, *245*, 308.
(53) Li, M. J.; Wu, Z. L.; Ma, Z.; Schwartz, V.; Mullins, D. R.; Dai, S.; Overbury, S. H. *J. Catal.* **2009**, *266*, 98.
(54) Fierro-Gonzalez, J. C.; Gates, B. C. *Catal. Today* **2007**, *122*, 201.
(55) Binet, C.; Daturi, M.; Lavalley, J. C. *Catal. Today* **1999**, *50*, 207.
(56) Li, M. J.; Wu, Z. L.; Overbury, S. H. *J. Catal.* **2011**, *278*, 133.
(57) Baron, M.; Bondarchuk, O.; Stacchiola, D.; Shaikhutdinov, S.; Freund, H. J. *J. Phys. Chem. C* **2009**, *113*, 6042.
(58) Vayssilov, G. N.; Lykhach, Y.; Migani, A.; Staudt, T.; Petrova, G. P.; Tsud, N.; Skala, T.; Bruix, A.; Illas, F.; Prince, K. C.; Matolin, V.; Neyman, K. M.; Libuda, J. *Nat. Mater.* **2011**, *10*, 310.
(59) Happel, M.; Myslivecek, J.; Johanek, V.; Dvorak, F.; Stetsovych, O.; Lykhach, Y.; Matolin, V.; Libuda, J. *J. Catal.* **2012**, *289*, 118.
(60) Camellone, M. F.; Fabris, S. *J. Am. Chem. Soc.* **2009**, *131*, 10473.
(61) Guzman, J.; Carrettin, S.; Corma, A. *J. Am. Chem. Soc.* **2005**, *127*, 3286.
(62) Shapovalov, V.; Metiu, H. *J. Catal.* **2007**, *245*, 205.
(63) Song, W.; Hensen, E. J. M. *Catal. Sci. Technol.* **2013**, *3*, 3020.
(64) Kim, H. Y.; Henkelman, G. *J. Phys. Chem. Lett.* **2013**, *4*, 216.
(65) Kim, H. Y.; Lee, H. M.; Henkelman, G. *J. Am. Chem. Soc.* **2012**, *134*, 1560.
(66) Ta, N.; Liu, J. Y.; Chenna, S.; Crozier, P. A.; Li, Y.; Chen, A. L.; Shen, W. J. *J. Am. Chem. Soc.* **2012**, *134*, 20585.
(67) Widmann, D.; Leppelt, R.; Behm, R. J. *J. Catal.* **2007**, *251*, 437.
(68) Widmann, D.; Behm, R. J. *Acc. Chem. Res.* **2014**, *47*, 740.
(69) Lee, Y.; He, G. H.; Akey, A. J.; Si, R.; Flytzani-Stephanopoulos, M.; Herman, I. P. *J. Am. Chem. Soc.* **2011**, *133*, 12952.
(70) Widmann, D.; Behm, R. J. *Angew. Chem., Int. Ed.* **2011**, *50*, 10241.

(71) Oberhauser, W.; Lavacchi, A.; Vizza, F.; Capozzoli, L.; Lee, H. M. *Appl. Catal., A* **2013**, *451*, 58.
(72) Lopez-Acevedo, O.; Kacprzak, K. A.; Akola, J.; Hakkinen, H. *Nat. Chem.* **2010**, *2*, 329.
(73) Ide, M. S.; Davis, R. J. *Acc. Chem. Res.* **2014**, *47*, 825.
(74) Mihaylov, M.; Ivanova, E.; Hao, Y.; Hadjiivanov, K.; Gates, B. C.; Knozinger, H. *Chem. Commun.* **2008**, 175.
(75) Bartholomew, C. H. *Studies in Surface Science and Catalysis*; Elsevier: Amsterdam, 1987; Vol. *34*, p 81.
(76) Chen, J.; Zhang, Q. F.; Bonaccorso, T. A.; Williard, P. G.; Wang, L. S. *J. Am. Chem. Soc.* **2014**, *136*, 92.